ACS APPLIED NANO MATERIALS

www.acsanm.org

Article

# Effect of Native Oxide on Stress in Silicon Nanowires: Implications for Nanoelectromechanical Systems

Mohammad Nasr Esfahani,[♦] Sina Zare Pakzad,[♦] Taotao Li, XueFei Li, Zuhal Tasdemir, Nicole Wollschläger, Yusuf Leblebici, and B. Erdem Alaca*

Cite This: *ACS Appl. Nano Mater.* 2022, 5, 13276−13285

Read Online

ACCESS | Metrics & More | Article Recommendations

**ABSTRACT:** Understanding the origins of intrinsic stress in Si nanowires (NWs) is crucial for their successful utilization as transducer building blocks in next-generation, miniaturized sensors based on nanoelectromechanical systems (NEMS). With their small size leading to ultrahigh-resonance frequencies and extreme surface-to-volume ratios, silicon NWs raise new opportunities regarding sensitivity, precision, and speed in both physical and biochemical sensing. With silicon optoelectromechanical properties strongly dependent on the level of NW intrinsic stress, various studies have been devoted to the measurement of such stresses generated, for example, as a result of harsh fabrication processes. However, due to enormous NW surface area, even the native oxide that is conventionally considered as a benign surface condition can cause significant stresses. To address this issue, a combination of nanomechanical characterization and atomistic simulation approaches is developed. Relying only on low-temperature processes, the fabrication approach yields monolithic NWs with optimum boundary conditions, where NWs and support architecture are etched within the same silicon crystal. Resulting NWs are characterized by transmission electron microscopy and micro-Raman spectroscopy. The interpretation of results is carried out through molecular dynamics simulations with ReaxFF potential facilitating the incorporation of humidity and temperature, thereby providing a close replica of the actual oxidation environment—in contrast to previous dry oxidation or self-limiting thermal oxidation studies. As a result, consensus on significant intrinsic tensile stresses on the order of 100 MPa to 1 GPa was achieved as a function of NW critical dimension and aspect ratio. The understanding developed herein regarding the role of native oxide played in the generation of NW intrinsic stresses is important for the design and development of silicon-based NEMS.

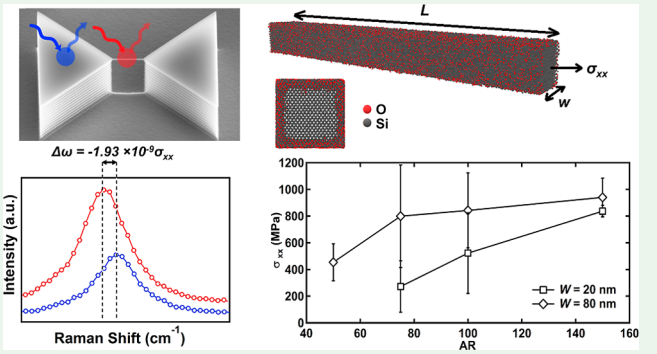


**KEYWORDS:** *nanoelectromechanical systems (NEMS), silicon nanowires, native oxide, intrinsic stress, Raman spectroscopy, molecular dynamics*



## INTRODUCTION

Nanowires (NWs) are considered as the central building blocks of a series of disruptive technologies and device concepts addressing a wide range of applications in nanoelectronics[1,2] and nanoelectromechanical systems (NEMS) such as mass spectrometers[3,4] and biomedical and physical sensors.[5−7] Silicon NWs (Si NWs) have received a particular attention in NEMS due to their high sensitivity, ease of integration, and compatibility with integrated circuits (ICs).[8,9] Mechanical stresses are especially critical in this respect, as they are known to contribute to the optoelectromechanical performance of Si NWs. For example, inducing tensile strain in Si NWs is reported to enhance transconductance[10,11] and improve thermal[12] and optical properties.[13] Such intrinsic stresses can lead to buckling of suspended Si NWs[14] with a direct impact on their mechanical behavior.[15] The intrinsic stress can also change the dopant diffusion mechanisms in Si NWs.[16] Furthermore, with piezoresistivity as the leading transduction technique in NEMS,[17] the characterization of embedded stresses in these miniscule structures becomes a technologically relevant task and an immediate challenge for the use of Si NWs in sensors.

For this purpose, Raman spectroscopy is widely employed to measure uniaxial stresses in NWs[18−20] with a series of studies specifically addressing Si NWs.[11,21−23] Although Raman techniques have demonstrated a strain up to 4.5% in Si NWs patterned on highly strained silicon-on-insulator (sSOI)

**Received:** July 8, 2022
**Accepted:** September 6, 2022
**Published:** September 15, 2022

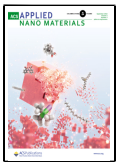

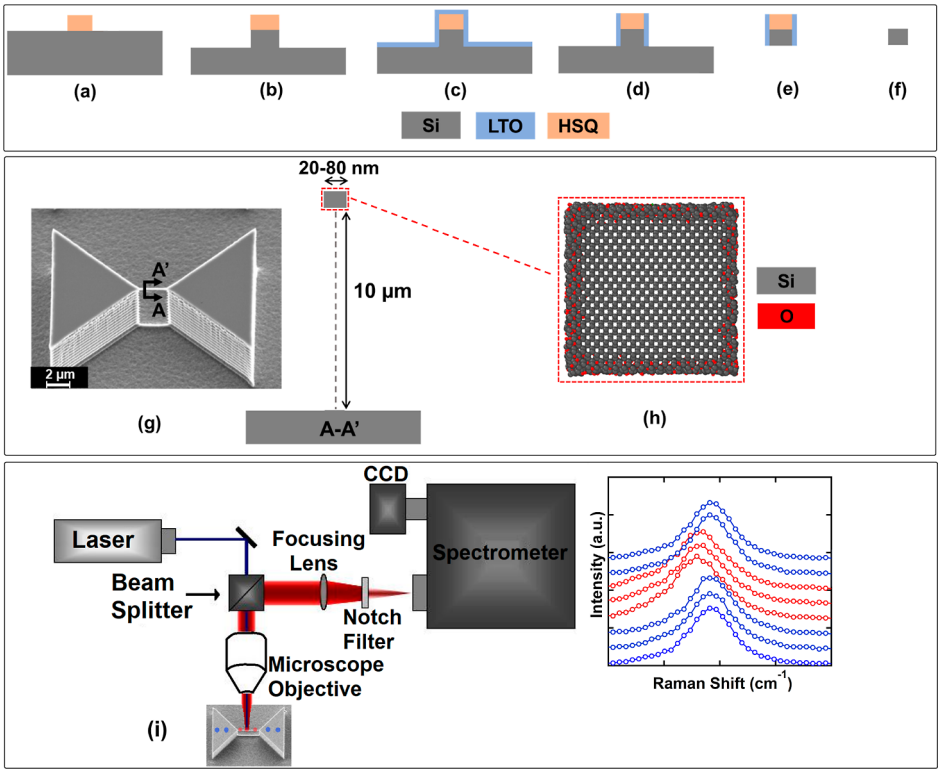


**Figure 1.** (a–f) Process flow for suspended Si NWs. (a) High-resolution patterning through electron beam lithography. (b) Anisotropic etching step forming the surface protrusion, the precursor line for the future Si NW. (c) Conformal coating of LTO. (d) LTO removal from horizontal surfaces. (e) DRIE with adequate undercut to release the Si NW. (f) Etching of protective layers. (g) Electron micrograph of a Si NW anchored between two 10 $\mu$m-thick triangular supports along with a schematic—not drawn to scale—showing the multiscale architecture in the A–A′ cross section. (h) Schematic representation of Si NW cross section with native oxide (Si and oxygen atoms are shown as gray and red spheres, respectively.) (i) Raman measurement setup consists of a laser source integrated with a beam splitter and a microscope, providing a spot size of 1 $\mu$m. A set of data obtained at locations indicated by blue and red dots on the micrograph is also provided as a plot of intensity vs Raman shift.

substrates,[11,21,22,24] the level of strain reported for Si NWs fabricated on stress-free substrates is limited to 0.048%.[23] In addition to Raman spectroscopy, X-ray diffraction approaches have been utilized to measure strain in Si NWs. For example, a strain rate of 0.04% was measured, whose origin was traced back to the catalyst residues used during the growth processes.[25,26] Recently, a scanning X-ray diffraction microscopy technique was employed for mapping in-plane crystalline strain in suspended Si NWs, reporting a strain level of 0.025%.[27]

Regarding the origin of the intrinsic stress, the formation of the native oxide layer on the Si NW surface has to be studied as one of the major causes in addition to stress generation due to fabrication processes such as reactive ion etching (RIE), die bonding, and wafer bonding.[12,28−30] The presence of native oxide is of paramount importance in Si NWs compared to larger Si structures utilized in microelectromechanical systems (MEMS), as the oxide thickness becomes comparable to the critical dimensions (CDs) of the nanostructure.[14,29,30] For example, the effect of native oxide on the mechanical behavior of Si nanoresonators was linked to dissipation mechanisms[31] and initial stresses.[28] As native oxide is a very thin layer of amorphous $SiO_2$ forming on Si surfaces at ambient temperatures upon contact with air, it has an entirely different growth mechanism compared to that of thermal oxides.[32,33] In this respect, previous works reported a strain up to 0.05% in Si NWs, which increases to 0.5%[34] or 160 MPa[15] of stress in thermally oxidized Si NWs depending on their surface condition. The initial formation of the native oxide layer on Si surfaces and the kinetics of its growth have been the subject of various studies, where parameters such as Si doping level, NW shape, and crystal orientation were found to alter the thickness of the oxide layer in a range between 0.3 and 5 nm.[35−37] The intrinsic stress in Si NWs has been predominantly the main focus of various studies, where prestrained substrates and thermally oxidized processes are used for fabrication.[11,21] Although a limited number of studies have presumed native oxide as a possible cause of intrinsic stress,[12,28−30] an in-depth study dedicated specifically to NWs is required to closely examine this link.

Understanding the role played by native oxide on the generation of intrinsic stress is a critical aspect of the future use of NWs as mechanical building blocks and will thus contribute to the transition from MEMS to NEMS as a high-precision sensor platform of ultimate miniaturization. For this purpose, a recently developed monolithic technology based on low-temperature processes is employed to fabricate Si NWs suspended between two microscale supports.[38] Micro-Raman spectroscopy is used to measure the uniaxial stresses in the Si NWs. Finally, an interpretation through modeling is achieved using reactive molecular dynamics (MD) for native oxide formation and intrinsic stress quantification. In the remainder of this work, the fabrication method will be discussed first followed by the micro-Raman measurement technique. After describing MD simulations, the work is concluded with a discussion on the native-oxide-induced stress in Si NWs.


https://doi.org/10.1021/acsanm.2c02983
ACS Appl. Nano Mater. 2022, 5, 13276−13285

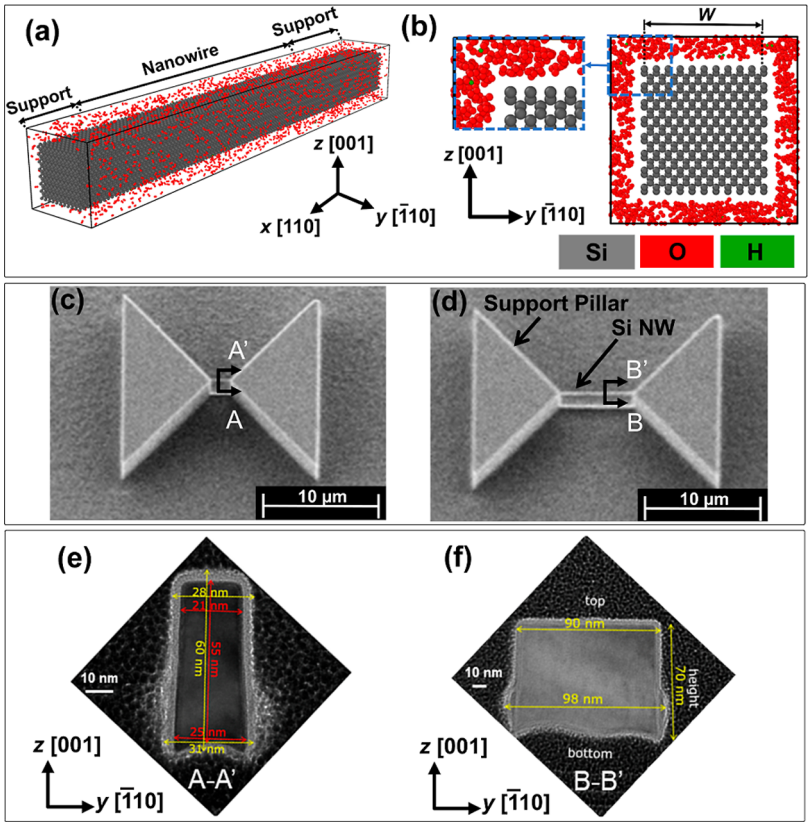


**Figure 2.** (a) Schematic showing the MD simulation of a Si NW with oxygen and water molecules resembling ambient oxidation under 42% humidity. Silicon, oxygen, and hydrogen atoms are represented with gray, red, and green spheres, respectively. (b) Cross-sectional image of a Si NW of width $W$ with its long axis in ⟨110⟩. SEM images of Si NWs with a (c) nominal width, $W$, of 20 nm and a length of 1.5 $\mu$m and a (d) nominal width, $W$, of 80 nm and a length of 6 $\mu$m, suspended between triangular micropillars. Cross-sectional TEM images of Si NWs with nominal widths, $W$, of (e) 20 nm and (f) 80 nm reveal the dimensions of the Si core as well as the native oxide envelope.

## MATERIALS AND METHODS

**Fabrication.** This study uses a recently developed monolithic method to fabricate Si NWs suspended between two microscale pillars.[38,39] The fabrication process starts with a p-type, ⟨100⟩ Si wafer of 100 mm diameter, 525 $\mu$m thickness, and a resistivity range of 0.1−100 Ω cm. In this process, 33 nanoscale features are patterned using electron beam (e-beam) lithography in a 200 nm-thick hydrogen silsesquioxane (HSQ) resist (Figure 1a). Then, the substrate is etched via RIE in $Cl_2$ plasma to form a Si protrusion on the surface (Figure 1b). The e-beam lithography defines the NW width, while the RIE process determines the same thickness for all patterned nanoscale features regardless of their in-plane dimension. The process is followed by the coating of a low-temperature oxide (LTO) film as the passivation layer via low-pressure chemical vapor deposition (Figure 1c). The LTO layer is then removed from lateral surfaces in a fluoroform plasma using inductively coupled plasma-based etching (Figure 1d). The Si protrusion, which will turn into a Si NW at the end of the process, is protected over all of its three surfaces. This is followed by deep reactive ion etching (DRIE) that releases the protrusion in the form of a Si NW (Figure 1e). This is achieved as undercuts associated with DRIE scallops from both sides are extensive enough to completely remove the Si column that extends beneath the Si surface protrusion. It is this same DRIE process during which pillars that serve as microscale support columns of the Si NWs are also generated. Finally, the e-beam resist and LTO film encapsulating NWs are removed by HF vapor etching (Figure 1f). Figure 1g demonstrates the multiscale nature of the fabrication technology as structures with a 3-order-of-magnitude scale difference are obtained in a single batch. The technique was previously shown to work successfully up to an etch depth of 40 $\mu$m,[40] and its various applications in MEMS[41,42] and nanomechanical resonators[43] were demonstrated. One sample Si NW suspended 10 $\mu$m above the substrate surface is shown in the micrograph in Figure 1g. Si NW surfaces then gradually oxidize, as a result of which Si NW assumes the cross section presented in Figure 1h. The presence of the uniform native oxide layer around the Si core was previously demonstrated in a cross-sectional transmission electron microscopy (TEM) study[44] and will be further elaborated below.

**Raman Measurement.** In order to quantify the intrinsic stress in suspended Si NWs, a home-built micro-Raman setup is employed with a Princeton Instruments SP-2500 spectrometer as shown in Figure 1i. A laser with a wavelength of 488 nm is used as the excitation source. The laser beam is passed to a beam splitter, followed by a microscope objective lens to create a spot size of 1 $\mu$m. The scattered light is collected through a focusing lens, passed into a notch filter, and then guided to the spectrometer. The microscope integrated with the measurement setup enables focusing of the microspot on NWs and facilitates a line scanning system to analyze the Raman shift along the entire length of suspended Si NWs with a high spatial resolution.

The Raman shift, $\Delta\omega$, is commonly used to measure stress by linking the longitudinal optical (LO) mode obtained in backscattering configuration with stress components in the Si NW.[21] In our case, $\Delta\omega$ is defined as the shift between the unstrained Si peak, $\omega_0$, and the LO shifted strained Si peak, $\omega_i$, as given in eq 1.

$$\begin{aligned}\Delta\omega &= \omega_i - \omega_0 \\ &= \frac{1}{2\omega_0}[[pS_{12} + q(S_{11} + S_{12})](\sigma_{xx} + \sigma_{yy}) \\ &\quad + (pS_{11} + 2qS_{12})\sigma_{zz}] \end{aligned} \tag{1}$$



https://doi.org/10.1021/acsanm.2c02983
ACS Appl. Nano Mater. 2022, 5, 13276−13285

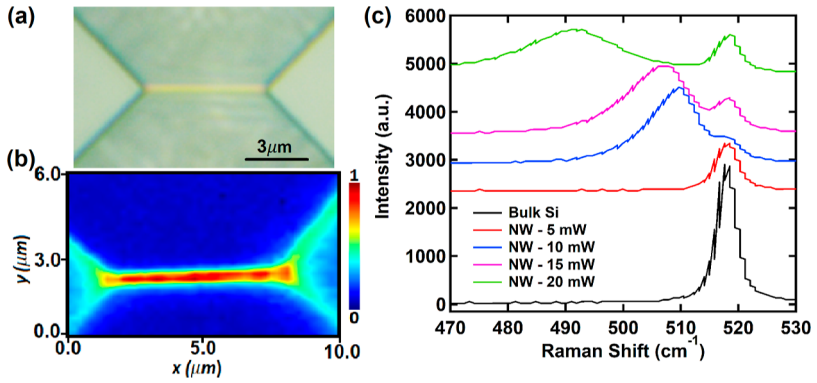


**Figure 3.** (a) Optical micrograph of a Si NW with a width of 80 nm and a length of 6 $\mu$m. (b) Mapped Raman intensity of the NW. (c) Raman spectra of bulk Si and the Si NW for a set of laser powers.

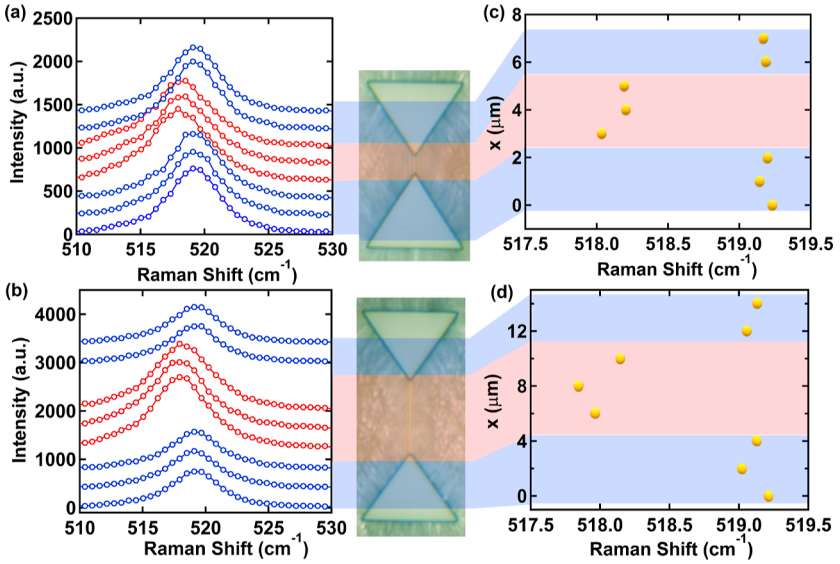


**Figure 4.** Raman spectra measured through a line scan on suspended Si NWs with widths of (a) 20 and (b) 80 nm and an AR of 75. Insets show the corresponding micrographs, where blue and red indicate micropillars and Si NW, respectively. Raman shifts extracted from panels (a,b) are provided with the same color code in (c,d), respectively.

where $S_{11}$ and $S_{12}$ are the elastic constants and $p$ and $q$ are the phonon deformation profiles. This model is valid for samples with negligible shear stress with $\sigma_{xx}$, $\sigma_{yy}$, and $\sigma_{zz}$ representing normal stress components along $x$, $y$, and $z$ directions, respectively. For a NW along the $x$ axis, $\sigma_{yy}$ and $\sigma_{zz}$ are negligible and eq 1 can be simplified as

$$\Delta\omega = \frac{1}{2\omega_0}[[pS_{12} + q(S_{11} + S_{12})]]\sigma_{xx} = (\mathrm{SSC})\sigma_{xx} \tag{2}$$

Relating the Raman shift to the uniaxial stress along the NW, the stress shift coefficient (SSC) of eq 2 is an important parameter. A wide range of SSC is reported for Si NWs, where the SSC of $-1.93 \times 10^{-9}$ cm$^{-1}$ Pa$^{-1}$ is recommended for NWs in sub-100 nm thickness.[21] Therefore, the Raman shift given in eq 2 can be written as

$$\Delta\omega\ [\mathrm{cm}^{-1}] = -1.93 \times 10^{-9} \times (\sigma_{xx}[Pa]) \tag{3}$$

**Atomic Simulations.** In the final phase of fabrication, Si NWs encapsulated within various oxide layers (e-beam resist, HSQ, and LTO) are treated in HF vapor as discussed in relation to Figure 1f. After this stage, the Si NW surfaces exposed to ambient conditions gradually oxidize. This oxide coating and the crystalline nature of the Si core were verified previously in a high-resolution TEM study.[44] To study the effect of the resulting structure on Si NW intrinsic stresses, MD simulations are carried out. To this end, the oxidation of ⟨110⟩ Si NWs is modeled using the reactive force field (ReaxFF) interatomic potential.[45] A detailed description of the force field as developed for Si−$SiO_2$ can be found elsewhere.[46−48] The force field parameters employed by Newsome et al.[49] are used in this work. The choice of ReaxFF is based on the fact that it has been parameterized and previously proven to accurately describe the oxide formation process by oxygen and water molecules.[49] A similar oxidation mechanism previously implemented by Khalilov et al.[48,50] on Si surfaces is utilized here to obtain native oxide formation at ambient temperature with humidity effect. In this model, Si NWs, oxygen, and water molecules (42% relative humidity) are defined in a periodic simulation box as depicted in Figure 2a,b. Both ends of the NW are fixed to mimic the type of support in the fabricated architecture of Figure 1g. The simulation box is relaxed at a temperature of 25 °C and under a pressure of 1 atm for 600 ps using the isobaric ensemble ($NPT$) with a time step of 1 fs. The resulting stress state in the Si NW, $\pi_{ij}$, is then calculated using the virial theorem[51] as

$$\sigma_{ij} = \frac{1}{2\Omega_o}\left[\sum_{\alpha=1}^{N}\sum_{\beta\neq\alpha}^{N}\frac{1}{r^{\alpha\beta}}\frac{\partial V(r^{\alpha\beta})}{\partial r}(v_i^{\alpha\beta}v_j^{\alpha\beta})\right] \tag{4}$$

where $\Omega_0$ stands for the atomic volume in an undeformed system with $N$ as the total number of atoms. Atomic distances between atoms $\alpha$ and $\beta$ are represented as $r^{\alpha\beta}$. $v_j^{\alpha}$ stands for the position of atom $\alpha$ along the $j$ direction, that is, $v_j^{\alpha\beta} = v_j^{\alpha} - v_j^{\beta}$ and $V$ represents the interatomic potential.



https://doi.org/10.1021/acsanm.2c02983
ACS Appl. Nano Mater. 2022, 5, 13276−13285

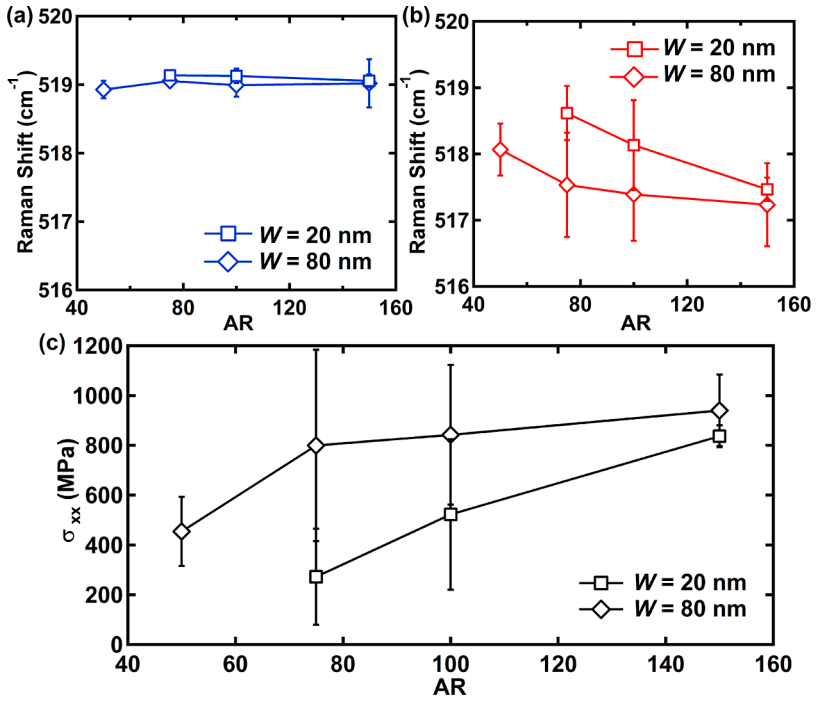


**Figure 5.** Raman peak shifts obtained in line scans as a function of AR for (a) micropillar supports and (b) suspended NWs. (c) Uniaxial stress in suspended Si NWs as a function of AR.

## RESULTS AND DISCUSSION

Si NWs with nominal widths ($W$) of 20 and 80 nm are fabricated with aspect ratios (ARs) of 75, 100, and 150, where AR is defined by the NW length-to-width ratio. Thanks to this chosen set of CDs, the results of this study remain relevant both for the application of Si-based nanoelectromechanical systems[3,4] and for the verification through atomistic simulations. NWs are suspended 10 $\mu$m above the substrate surface and supported by microscale pillars at both ends. Micrographs in Figure 2c,d depict Si NWs with $W$ values of 20 and 80 nm, respectively. Both NWs have an AR of 75 translating into a Si NW length of 1.5 $\mu$m in Figure 2c and 6 $\mu$m in Figure 2d. The cross section of each NW is also studied as presented by the corresponding lower micrographs (TEM images). An initial protrusion with a thickness of about 70 nm obtained during the RIE process (Figure 1b) leads to rectangle and square cross sections of NWs with nominal widths of 20 and 80 nm, respectively. Both micrographs exhibit a uniform native oxide layer of 3−3.5 nm thickness.

Raman measurements carried out on both types of NWs under ambient conditions are initiated through mapping scattered beams for Si NWs and micropillars. The optical microscope in the Raman measurement setup is a navigation system for laser beam positioning. Figure 3a depicts one such optical image of the Si NW of Figure 2d. The resulting normalized Raman intensity obtained for this Si NW is shown in Figure 3b. This indicates a successful confocal beam scattering from the suspended NW, and hence, the obtained spectra can be considered for calculating the NW Raman shift. In the next step, laser-related effects are eliminated from Raman measurements, where the laser power can cause a Raman shift due to local heating of the NW.[52] In this respect, Raman measurements are carried out on NWs with a series of different laser powers, whose results are then compared with those of the bulk Si (Figure 3c). A significant heat effect is observed for any laser power in excess of 5 mW. To eliminate heating effects, all Raman measurements are carried out at a power of 2 mW.

After the calibration of the laser power, line scans are carried out along NWs measuring the Raman shift of the bulk as well as the NW. Raman spectra for the NW in the $x$-direction are recorded, which corresponds to a line scan along the NW as shown in Figure 3b with the associated Raman intensity. Figure 4a,b exhibits the Raman spectra obtained from such line scans of Si NWs with $W$ values of 20 and 80 nm, respectively. The shaded colors defined on the attached micrographs indicate the location of Raman spectra measured through a line scan, where blue and red curves represent micropillars and Si NWs, respectively. The Gaussian model is used for fitting the Raman peaks of NWs under tension,[53] while the Lorentzian line shape is considered mainly for homogeneous systems.[53,54] In this respect, the Gaussian fit is employed here to predict the Raman shift in a line scan. Figure 4c,d exhibits the Raman shifts with the same color code along the NW longitudinal axis ($x$-direction) for the 20 and 80 nm NW, respectively. A fairly narrow distribution of the peaks is obtained in both cases. Results show Raman spectra with a peak intensity at 519.1 cm$^{-1}$ on Si micropillars, while spectra from suspended NWs shift toward lower wavenumbers. An average downshift of 1.0 cm$^{-1}$ is observed for both NWs. This shift toward lower wavenumbers indicates a tensile intrinsic stress along the NW axis.

Finally, Raman spectra for each NW of different ARs are obtained by the same line scan measurement technique. Gaussian fits are performed on the data to estimate the Raman peak shift for each spectrum. Figure 5 shows the resulting Raman shifts for micropillars and suspended NWs as a function of AR. A total of 33 NWs are tested for proper statistical treatment of the findings as reflected by the error bars of Figure 5. Results in Figure 5a indicate a Raman peak of 519.0 ± 0.3 cm$^{-1}$ for micropillars regardless of NW size. On


https://doi.org/10.1021/acsanm.2c02983
ACS Appl. Nano Mater. 2022, 5, 13276−13285

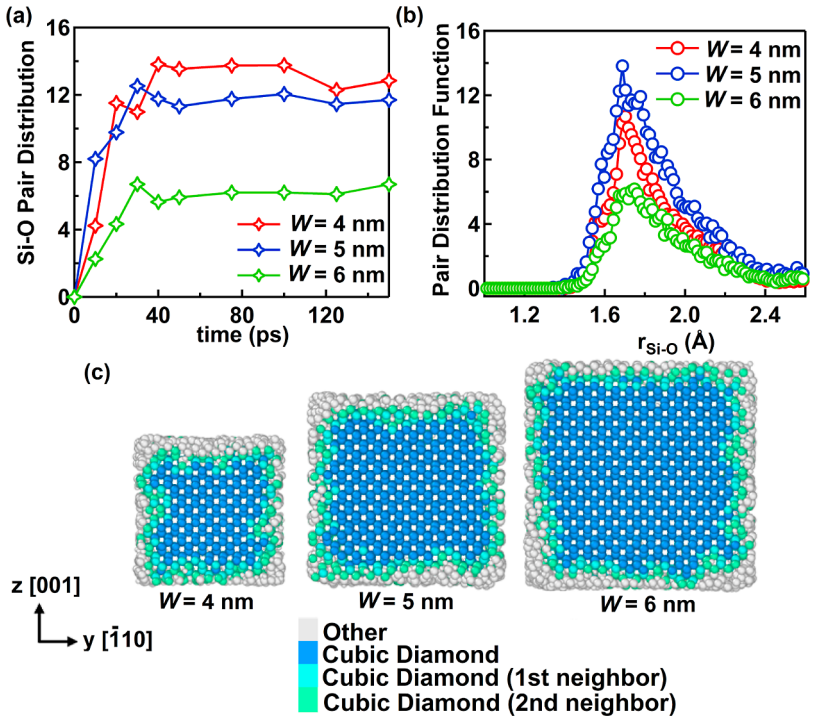


**Figure 6.** (a) Magnitude of the Si−O pair distribution as a function of time (AR = 7.5) and (b) PDF of Si−O for Si NWs at 40 ps. (c) Atomic structure of Si NWs upon oxidation. Diamond cubic crystal structure is retained within the crystalline core of the Si NW.

the contrary, a lower Raman peak shift is observed for Si NWs with increasing NW AR (Figure 5b). In this respect, the Raman shift in Si NWs with $W$ = 80 nm reduces from 518.0 to 517.2 $cm^{-1}$ with the AR changing from 50 to 150. Compared to NWs with $W$ = 80 nm, a larger change in the Raman shift is obtained in Si NWs with $W$ = 20 nm, where increasing AR from 75 to 150 reduces the Raman peak shift from 518.6 $cm^{-1}$ to 517.4 $cm^{-1}$.

At this stage, the uniaxial stress in Si NWs can be calculated via eq 3. Figure 5c depicts the resulting uniaxial stress values as a function of AR. A tensile stress of 431 MPa is obtained for Si NWs with a $W$ value of 80 nm and an AR of 50, while it reaches 892 MPa for an AR of 150. A similar size-dependent uniaxial stress is observed for Si NWs with a $W$ value of 20 nm, where the tensile stress increases from 258 MPa to 794 MPa with the AR increasing from 75 to 150. Compared to the measurement uncertainty, the trends exhibited for NWs with different widths are found to be significant with the highest standard deviations of 364 and 287 MPa obtained for $W$ values of 80 and 20 nm, respectively. This stress range corresponds to an intrinsic strain of up to 0.5 ± 0.2%.

It is to be emphasized that the associated fabrication technology is based on low-temperature, top-down processes on Si substrates to minimize any fabrication-induced stresses in Si NWs, while previous studies reporting residual stresses in Si NWs employed pre-strained substrates[11,21,22] or used high-temperature processes.[12] Some studies presumed native oxide formation as the origin of intrinsic stress in Si NWs,[12,29,30] where the transition in the crystal structure between amorphous $SiO_2$ to crystalline Si is attributed to the residual stresses in NWs.[28,29] To the best of our knowledge, findings in this work represent the first study reporting intrinsic stresses in top-down Si NWs fabricated neither via high-temperature processes nor using pre-strained substrates.

It is observed that the strain levels reported here are comparable to those reported by a number of previous studies on top-down fabricated Si NWs using high-temperature processes,[12] while the measured strain in this study is significantly lower than those works using pre-strained substrates.[11,21,22] However, it remains significant compared to others, especially those achieved through X-ray diffraction techniques.[27] Although lower strain levels on the order of 0.025% were reported by the latter, an important tilt magnitude in the crystal lattice was detected.[27] The difference between the nature of X-ray and Raman measurements previously attracted attention in the field of intrinsic stress measurement of nanostructures.[55] Such discrepancies can be linked to differences between the measurement methods, effects of diffuse scattering, and defect state of the material and surface defects.

Apart from the intrinsic stress magnitude, the effect of NW size surfaced as another observation that was not reported before. Data in Figure 5c reveals clear trends regarding the size effect, where increasing both NW width, $W$, and AR leads to higher intrinsic stresses. The effect of AR is especially significant for smaller, that is, $W$ = 20 nm, NWs. Regarding the NW width, previous studies using pre-strained substrates and high-temperature processes reported the opposite trend as a function of $W$.[11,14] The expansion during the thermal oxidation process at high temperatures and associated stresses are considered as the main contributing factors for such intrinsic stresses in Si NWs.[12] The residual stresses as a direct impact of lithography resist curing[56] and LTO deposition[57] are found to be negligible compared to the stresses measured in this study. Furthermore, compressive stresses are reported as a result of etching processes in Si nanostructures.[58] Thus, high tensile stresses encountered in this work verify that the surface state—rather than the fabrication itself—is responsible for the generation of intrinsic stresses. Representing the state of the


https://doi.org/10.1021/acsanm.2c02983
ACS Appl. Nano Mater. 2022, 5, 13276−13285

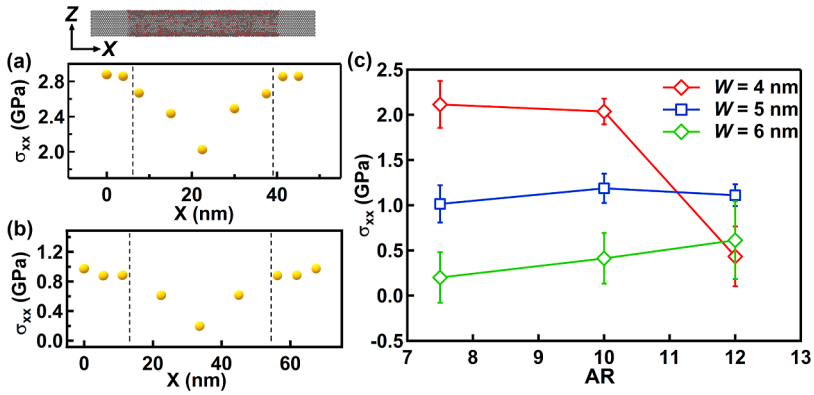


**Figure 7.** Sample stress distributions along Si NWs with an AR of 7.5 and *W* values of (a) 4 and (b) 6 nm. Significant tensile stresses are observed with their magnitude decreasing with increasing *W*. (c) MD prediction of average uniaxial stress in Si NWs as a function of AR. Stress level increases significantly with reducing *W*.

art, the present technology comes as close to eliminating fabrication-related stresses as possible. To our knowledge, there is no top-down alternative that would match the success of this technology in thick SOI wafers.

Taking the aforementioned indicators into consideration, the formation of native oxide on Si NW surfaces following the final oxide removal step of Figure 1f via HF vapor etch is considered as the main reason behind the observed tensile stresses in this work. Therefore, MD simulations are employed to study the effect of surface oxidation on the generation of intrinsic stresses in suspended Si NWs. Such simulations can serve as a powerful tool for the interpretation of the above measurement results, as—to the best of our knowledge—no previous MD treatment of the native oxide growth problem exists for Si NWs. Prior MD studies focused on native oxide growth mechanisms investigating chemical composition (stoichiometry),[59] incident particle impact (oxygen atom or oxygen molecule),[60] and oxide thickness,[61] while the majority mainly focused on the stresses in thermally oxidized Si NWs.[36,62,63] Moreover, a series of studies employed MD to model stress distribution in the Si−$SiO_2$ interface, reporting a compressive stress concentrated on the oxide region in the vicinity of the interface.[62] In addition, the ReaxFF potential was employed to model thermal oxide formation on Si NWs using chemical reactions at high temperatures up to 1200 K. A compressive stress of 7−8 GPa was reported in thermal oxide, while Si NWs were found to be under a tensile stress of 2−3 GPa.[59] Another study modeled the interfacial stresses during self-limiting oxidation of Si NWs, reporting a change in the residual stress from 3.2 GPa to 2 GPa by increasing the temperature from 300 up to 700 K.[60]

In contrast to MD studies on thermal oxidation, the present study employs the ReaxFF potential to model the native oxide formation under ambient conditions, replicating the oxidation after etching of protective layers during the fabrication process shown in Figure 1f, where Si NWs are doubly clamped between micropillars. For this purpose, reactive MD simulations are carried out on Si NWs with both ends fixed over a certain support region, whose length is set to 1/8th of NW length, replicating the fixed−fixed boundary condition for the Si NW. The periodic boundary condition is defined along all directions. In the first step, the oxide formation on Si NW surfaces is studied through measuring pair distribution functions (PDFs). Figure 6a demonstrates the magnitude of the pair distribution for Si−O bonds over the simulation time. Oxidation starts off over the first 20 ps with a high rate and reaches the steady state after 60 ps for all *W* values involved. Figure 6b depicts the PDF of Si−O bonds at 40 ps as a function of bond length ($r_{Si-O}$). A peak at 1.7 Å is observed for the PDF of oxide. An average Si−O bond length was reported previously as about 1.60 Å using MD simulations,[64] while bond length measurements yield values between 1.55 and 1.75 Å for different polymorphs of $SiO_2$.[65] The native oxide thickness is measured using the diamond crystal structure analysis while identifying the core Si and native oxide regions.[66] Figure 6c demonstrates the diamond cubic crystal in core Si, while an amorphous native oxide layer is formed around NWs. Results show a native oxide with a thickness ranging between 0.5 and 1.1 nm, encapsulating the Si crystal, which is comparable to previous experimental observations[37,67,68] as well as MD simulations.[50,59,60,62,69]

Once the oxidation process reaches its steady state, atomic stresses are computed along the longitudinal direction (*x*-axis) as described by eq 4. Figure 7a,b depicts the distribution of this uniaxial stress component for AR = 7.5. For *W* = 4 nm (Figure 7a), an average tensile stress of 2.9 GPa is observed along the support regions, while this tensile stress drops to an average value of 2.3 GPa within the NW zone. Although there is a certain variation in $\sigma_{xx}$, as it drops from 2.6 GPa at the fixed end of the NW zone to 2.0 GPa at the midspan, there is a clear reduction compared to the stress within the support region. The same trend is obtained for Si NWs of *W* = 6 nm (Figure 7b), where a tensile stress of 1.0 GPa obtained in the support region drops to 0.2 GPa within the NW. Raman measurements of Figure 4 can be successfully captured by oxidation simulations at room temperature. Hence, both the sign and magnitude of the stress induced through the formation of native oxide around a Si NW can be captured by reactive MD simulations. In contrast to previous studies based on high-temperature (thermal) oxidation, the present approach uses reactive atomic simulations for capturing the native oxide growth on Si NWs at the end of the fabrication process (following Figure 1f) at room temperature. Although there is an order of magnitude scale difference between fabricated Si NWs and atomic simulations, both experimental and modeling studies yielded stresses of the same sign, that is, tensile, and order, that is, 100 MPa to 1 GPa. Having employed the state-of-the-art fabrication, measurement, and computational tools, this scale difference is kept at a minimum. With such verification, the resulting effect of native oxide formation is


https://doi.org/10.1021/acsanm.2c02983
ACS Appl. Nano Mater. 2022, 5, 13276−13285

established as a significant and relevant issue for the performance of Si-based nanoelectromechanical systems.

After calculating the stress profile along Si NWs through reactive MD simulations, the size effect is similarly studied by plotting average $\sigma_{xx}$ as a function AR (Figure 7c). A considerable size-dependent stress is evident for Si NWs with $W$ less than 6 nm. The uniaxial stress changes from 2.1 to 0.4 GPa with the AR increasing from 7.5 to 12 for $W$ = 4 nm. The stress level reduces with increasing NW width, while its variations also become less sensitive to AR. The stress level observed in this work is comparable to previous MD studies on thermally oxidized Si NWs.[36,62,63] For instance, a tensile stress of 3−6 GPa is obtained in MD simulations of Si NWs with thermal oxide,[62] while a lower tensile stress in a range of 100 MPa to 2.0 GPa is predicted through finite element modeling of oxidized Si nanobeams.[36] Although trends in AR and $W$ dependence established here cannot directly translate into the observed behavior at the nanoscale, both experimental observations and MD simulations exhibit a considerable tensile stress as a result of native oxide formation in Si NWs. Hence, a strong link between the measured stress profiles obtained through micro-Raman technique (Figure 5c) and Si NW surface state is established, validating the hypothesis on native oxide effect considerations in a series of previous studies.[12,28−30] The use of a low-temperature monolithic technology has provided a direct link between the surface state and intrinsic stress measurements. The comparison of MD results with experimental data has revealed a series of similar trends. Measured stress levels are found to be comparable to those predicted by MD simulations. Here, atomic simulations are utilized to interpret and verify experimental observations on the effect of native oxide on stress in Si NWs. With work in both compartments carried out using state-of-the-art tools and techniques, an exemplary correspondence is obtained, although a series of further benchmark studies is required to understand the size effect on the mechanical properties of Si NWs and its implications for intrinsic stresses.

## CONCLUSIONS

Following the miniaturization trend in electronics as predicted by Moore's law, electromechanical systems are also under a similar transition fueled by the request for ultrafast and low-power sensors. With their small size leading to ultrahigh-resonance frequencies and extreme surface-to-volume ratios, Si NWs are leading candidates for transducer building blocks in next-generation, miniaturized sensors based on NEMS. Although top-down fabrication of Si NWs in NEMS follows the footsteps of transistor manufacturing, the associated challenges are unique, as extreme topographies have to be utilized, and hence, their full utilization necessitates rigorous technology development. In this respect, the role played by the native oxide on the generation of intrinsic stresses is a critical issue. Although its presence in MEMS can be neglected, Si NWs with their immense surface-to-volume ratio are affected by all surface conditions including the native oxide.

This study aims to investigate the impact of native oxide on the embedded stress in Si nanostructures. In this respect, a recently developed technology is utilized to fabricate suspended Si NWs, which involved a combination of high-resolution lithography and a two-stage etching. No high-temperature processes were utilized during fabrication, and pristine Si NWs were left to oxidize under ambient conditions after a final thorough cleaning stage involving HF vapor etching. This led to the formation of native oxide on all Si NW surfaces as verified by high-resolution TEM. Si NWs of two different nominal widths of 20 and 80 nm were fabricated with ARs of 75, 100, and 150. TEM measurements revealed a uniform native oxide layer of 3−3.5 nm thickness. For the characterization of intrinsic stresses in Si NWs, a micro-Raman spectroscopy-based approach was developed and applied to a set of 33 samples. A downshift was consistently observed in Si NWs, representing a tensile intrinsic stress. For 80 nm Si NWs, this tensile stress was observed to change from 431 to 892 MPa with increasing AR from 50 to 150. In parallel, a tensile stress of 258 MPa was observed for 20 nm Si NWs with an AR of 75, which increased to 794 MPa for an AR of 150. For the interpretation of measurements, a reactive MD simulation had to be developed for the modeling of the formation of native oxide around Si NWs. Si NWs with nominal widths of 4, 5, and 6 nm and ARs of 7.5, 10, 12, and 15 were modeled using the ReaxFF potential.

Results exhibited tensile stresses in the range of 100 MPa to 2.0 GPa. Both the sign and the magnitude of stresses induced by the formation of native oxide around a Si NW could thus be captured. Hence, experimental measurements and computational simulations indicate a significant tensile stress in Si NWs as a direct outcome of native oxide formation. It was shown for the first time that room-temperature formation of native oxide can generate significant stresses in Si NWs. This result was achieved through careful development of both the fabrication and modeling approaches, where the first suppresses any unintended sources of stress generation and ensures correct boundary conditions, while the latter—having taken temperature and humidity effects into account—provides a close replica of the oxidation environment under ambient conditions. Therefore, the simulation approach utilized here can replace those reported in previous dry oxidation or self-limiting thermal oxidation studies. The understanding developed herein regarding the role of native oxide played in the generation of Si NW intrinsic stresses is important for the design and development of future NEMS sensors.

## AUTHOR INFORMATION


### Corresponding Author

**B. Erdem Alaca** − *Department of Mechanical Engineering, n²STAR-Koç University Nanofabrication and Nanocharacterization Center for Scientific and Technological Advanced Research, and Koç University Surface Technologies Research Center (KUYTAM), Koç University, Istanbul 34450, Turkey;* orcid.org/0000-0001-5931-8134; Email: ealaca@ku.edu.tr

### Authors

**Mohammad Nasr Esfahani** − *School of Physics, Engineering and Technology, University of York, York YO10 5DD, U.K.;* orcid.org/0000-0002-6973-2205

**Sina Zare Pakzad** − *Department of Mechanical Engineering, Koç University, Istanbul 34450, Turkey;* orcid.org/0000-0002-7029-4812

**Taotao Li** − *School of Electronic Science and Engineering, Nanjing University, Nanjing 210093, China;* orcid.org/0000-0002-2815-3856

**XueFei Li** − *School of Electronic Science and Engineering, Nanjing University, Nanjing 210093, China*




https://doi.org/10.1021/acsanm.2c02983
ACS Appl. Nano Mater. 2022, 5, 13276−13285

**Zuhal Tasdemir** − *Laboratory of Micro and Nanotechnology, Paul Scherrer Institute, Villigen PSI CH-5232, Switzerland*
**Nicole Wollschläger** − *Department 5.1: Materialography, Fractography and Aging of Technical Materials, Bundesanstalt für Materialforschung und -prüfung (BAM), Berlin 12205, Germany*
**Yusuf Leblebici** − *Microelectronic Systems Laboratory, Swiss Federal Institute of Technology—Lausanne (EPFL), Lausanne CH-1015, Switzerland; Rectorate, Sabanci University, Istanbul 34956, Turkey*

Complete contact information is available at: https://pubs.acs.org/10.1021/acsanm.2c02983

### Author Contributions

♦M.N.E. and S.Z.P. contributed equally to this work.

### Notes

The authors declare no competing financial interest.

## ■ ACKNOWLEDGMENTS

S.Z.P. and B.E.A. gratefully acknowledge the financial support by Tubitak under grant no. 120E347.

## ■ REFERENCES

(1) Jia, C.; Lin, Z.; Huang, Y.; Duan, X. Nanowire electronics: from nanoscale to macroscale. *Chem. Rev.* **2019**, *119*, 9074−9135.
(2) Lu, W.; Lieber, C. M. Nanoelectronics from the bottom up. *Nanoscience And Technology: A Collection of Reviews from Nature Journals*; World Scientific, 2010; pp 137−146.
(3) Sage, E.; Sansa, M.; Fostner, S.; Defoort, M.; Gély, M.; Naik, A. K.; Morel, R.; Duraffourg, L.; Roukes, M. L.; Alava, T.; Jourdan, G.; Colinet, E.; Masselon, C.; Brenac, A.; Hentz, S. Single-particle mass spectrometry with arrays of frequency-addressed nanomechanical resonators. *Nat. Commun.* **2018**, *9*, 3283.
(4) Yang, Y.-T.; Callegari, C.; Feng, X.; Ekinci, K. L.; Roukes, M. L. Zeptogram-scale nanomechanical mass sensing. *Nano Lett.* **2006**, *6*, 583−586.
(5) Wang, Z.; Lee, S.; Koo, K.-i.; Kim, K. Nanowire-based sensors for biological and medical applications. *IEEE Trans. NanoBioscience* **2016**, *15*, 186−199.
(6) Sang, S.; Wang, Y.; Feng, Q.; Wei, Y.; Ji, J.; Zhang, W. Progress of new label-free techniques for biosensors: a review. *Crit. Rev. Biotechnol.* **2016**, *36*, 465−481.
(7) Ambhorkar, P.; Wang, Z.; Ko, H.; Lee, S.; Koo, K.-i.; Kim, K.; Cho, D.-i. D. Nanowire-based biosensors: from growth to applications. *Micromachines* **2018**, *9*, 679.
(8) Nasr Esfahani, M.; Alaca, B. E. A Review on Size-Dependent Mechanical Properties of Nanowires. *Adv. Eng. Mater.* **2019**, *21*, 1900192.
(9) Weber, W.; Heinzig, A.; Trommer, J.; Martin, D.; Grube, M.; Mikolajick, T. Reconfigurable nanowire electronics−a review. *Solid-State Electron.* **2014**, *102*, 12−24.
(10) Seike, A.; Tange, T.; Sugiura, Y.; Tsuchida, I.; Ohta, H.; Watanabe, T.; Kosemura, D.; Ogura, A.; Ohdomari, I. Strain-induced transconductance enhancement by pattern dependent oxidation in silicon nanowire field-effect transistors. *Appl. Phys. Lett.* **2007**, *91*, 202117.
(11) Minamisawa, R. A.; Süess, M. J.; Spolenak, R.; Faist, J.; David, C.; Gobrecht, J.; Bourdelle, K. K.; Sigg, H. Top-down fabricated silicon nanowires under tensile elastic strain up to 4.5%. *Nat. Commun.* **2012**, *3*, 1096.
(12) Fan, D.; Sigg, H.; Spolenak, R.; Ekinci, Y. Strain and thermal conductivity in ultrathin suspended silicon nanowires. *Phys. Rev. B* **2017**, *96*, 115307.
(13) Geiger, R.; Zabel, T.; Sigg, H. Group IV direct band gap photonics: methods, challenges, and opportunities. *Front. Mater.* **2015**, *2*, 52.
(14) Allain, P.; Le Roux, X.; Parrain, F.; Bosseboeuf, A. Large initial compressive stress in top-down fabricated silicon nanowires evidenced by static buckling. *J. Micromech. Microeng.* **2012**, *23*, 015014.
(15) Calahorra, Y.; Shtempluck, O.; Kotchetkov, V.; Yaish, Y. Young's modulus, residual stress, and crystal orientation of doubly clamped silicon nanowire beams. *Nano Lett.* **2015**, *15*, 2945−2950.
(16) Prüßing, J. K.; Böckendorf, T.; Kipke, F.; Xu, J.; Puranto, P.; Lundsgaard Hansen, J.; Bougeard, D.; Peiner, E.; Bracht, H. Retarded boron and phosphorus diffusion in silicon nanopillars due to stress induced vacancy injection. *J. Appl. Phys.* **2022**, *131*, 075702.
(17) Zhu, J.; Liu, X.; Shi, Q.; He, T.; Sun, Z.; Guo, X.; Liu, W.; Sulaiman, O. B.; Dong, B.; Lee, C. Development trends and perspectives of future sensors and MEMS/NEMS. *Micromachines* **2019**, *11*, 7.
(18) Nugent, K.; Prawer, S. Confocal Raman strain mapping of isolated single CVD diamond crystals. *Diamond Relat. Mater.* **1998**, *7*, 215−221.
(19) Wolf, I. Micro-Raman spectroscopy to study local mechanical stress in silicon integrated circuits. *Semicond. Sci. Technol.* **1996**, *11*, 139.
(20) Harris, S. J.; O'Neill, A. E.; Yang, W.; Gustafson, P.; Boileau, J.; Weber, W.; Majumdar, B.; Ghosh, S. Measurement of the state of stress in silicon with micro-Raman spectroscopy. *J. Appl. Phys.* **2004**, *96*, 7195−7201.
(21) Spejo, L.; Arrieta-Concha, J.; Puydinger dos Santos, M.; Barros, A.; Bourdelle, K.; Diniz, J.; Minamisawa, R. Non-linear Raman shift-stress behavior in top-down fabricated highly strained silicon nanowires. *J. Appl. Phys.* **2020**, *128*, 045704.
(22) Süess, M.; Minamisawa, R.; Geiger, R.; Bourdelle, K.; Sigg, H.; Spolenak, R. Power-dependent Raman analysis of highly strained Si nanobridges. *Nano Lett.* **2014**, *14*, 1249−1254.
(23) Park, S.; Rho, H.; Song, J.; Lee, S.-K.; Kim, G.-S.; Lee, C. Spatially-resolved and polarized Raman scattering from a single Si nanowire. *J. Raman Spectrosc.* **2015**, *46*, 524−530.
(24) Hashemi, P.; Gomez, L.; Hoyt, J. L. Gate-all-around n-MOSFETs with uniaxial tensile strain-induced performance enhancement scalable to sub-10-nm nanowire diameter. *IEEE Electron Device Lett.* **2009**, *30*, 401−403.
(25) Dupré, L.; Buttard, D.; Leclere, C.; Renevier, H.; Gentile, P. Gold contamination in VLS-grown Si nanowires: multiwavelength anomalous diffraction investigations. *Chem. Mater.* **2012**, *24*, 4511−4516.
(26) Buttard, D.; Gentile, P.; Renevier, H. Grazing incidence X-ray diffraction investigation of strains in silicon nanowires obtained by gold catalytic growth. *Surf. Sci.* **2011**, *605*, 570−576.
(27) Dolabella, S.; Frison, R.; Chahine, G. A.; Richter, C.; Schulli, T. U.; Tasdemir, Z.; Alaca, B. E.; Leblebici, Y.; Dommann, A.; Neels, A. Real-and Q-space travelling: multi-dimensional distribution maps of crystal-lattice strain ($\epsilon_0$44) and tilt of suspended monolithic silicon nanowire structures. *J. Appl. Crystallogr.* **2020**, *53*, 58−68.
(28) Beccari, A.; Visani, D.; Fedorov, S.; Bereyhi, M.; Boureau, V.; Engelsen, N.; Kippenberg, T. Strained crystalline nanomechanical resonators with quality factors above 10 billion. *Nat. Phys.* **2022**, *18*, 436.
(29) Toda, S.; Oishi, T.; Yoshioka, T.; Okuno, T. Optical properties of silicon nanowires fabricated by electroless silver deposition. *Jpn. J. Appl. Phys.* **2010**, *49*, 095002.
(30) Poborchii, V.; Tada, T.; Morita, Y.; Kanayama, T. Ultraviolet Raman spectra of single uncoated and SiO2-coated silicon-on-insulator nanowires: Phonon boundary scattering, wave-vector relaxation and stress. *Appl. Phys. Lett.* **2013**, *103*, 153104.
(31) Tao, Y.; Navaretti, P.; Hauert, R.; Grob, U.; Poggio, M.; C L Degen, C. L. Permanent reduction of dissipation in nanomechanical Si resonators by chemical surface protection. *Nanotechnology* **2015**, *26*, 465501.
(32) Morita, M.; Ohmi, T.; Hasegawa, E.; Kawakami, M.; Ohwada, M. Growth of native oxide on a silicon surface. *J. Appl. Phys.* **1990**, *68*, 1272−1281.

(33) Steinrück, H.-G.; Schiener, A.; Schindler, T.; Will, J.; Magerl, A.; Konovalov, O.; Li Destri, G.; Seeck, O. H.; Mezger, M.; Haddad, J.; Deutsch, M.; Checco, A.; Ocko, M. Nanoscale structure of Si/SiO2/organics interfaces. *ACS Nano* **2014**, *8*, 12676−12681.
(34) Takeuchi, T.; Tatsumura, K.; Shimura, T.; Ohdomari, I. X-ray diffraction study of strain distribution in oxidized Si nanowires. *J. Appl. Phys.* **2009**, *106*, 073506.
(35) Philipp, H. R.; Taft, E. An optical characterization of native oxides and thin thermal oxides on silicon. *J. Appl. Phys.* **1982**, *53*, 5224−5229.
(36) Han, X.-L.; Larrieu, G.; Krzeminski, C. Modelling and engineering of stress based controlled oxidation effects for silicon nanostructure patterning. *Nanotechnology* **2013**, *24*, 495301.
(37) McDowell, M. T.; Lee, S. W.; Ryu, I.; Wu, H.; Nix, W. D.; Choi, J. W.; Cui, Y. Novel size and surface oxide effects in silicon nanowires as lithium battery anodes. *Nano Lett.* **2011**, *11*, 4018−4025.
(38) Tasdemir, Z.; Peric, O.; Sacchetto, D.; Fantner, G. E.; Leblebici, Y.; Alaca, B. E. Monolithic fabrication of silicon nanowires bridging thick silicon structures. *IEEE Trans. Nanotechnol.* **2018**, *17*, 1299−1302.
(39) Zare Pakzad, S.; Nasr Esfahani, M.; Tasdemir, Z.; Wollschlaeger, N.; Li, X.; Li, T.; Yilmaz, M.; Leblebici, Y.; Alaca, B. E. A new characterization approach to study the mechanical behavior of silicon nanowires. *MRS Adv.* **2021**, *6*, 500−505.
(40) Esfahani, M. N.; Yilmaz, M.; Wollschläger, N.; Rangelow, I. W.; Leblebici, Y.; Alaca, B. E. Monolithic technology for silicon nanowires in high-topography architectures. *Microelectron. Eng.* **2017**, *183*, 42−47.
(41) Esfahani, M. N.; Leblebici, Y.; Alaca, B. E. A monolithic approach to downscaling silicon piezoresistive sensors. *J. Microelectromech. Syst.* **2017**, *26*, 624−631.
(42) Yilmaz, M.; Kilinc, Y.; Nadar, G.; Tasdemir, Z.; Wollschläger, N.; Österle, W.; Leblebici, Y.; Alaca, B. E. Top-down technique for scaling to nano in silicon MEMS. *J. Vac. Sci. Technol., B: Nanotechnol. Microelectron.: Mater., Process., Meas., Phenom.* **2017**, *35*, 022001.
(43) Esfahani, M. N.; Kilinc, Y.; Karakan, M. Ç.; Orhan, E.; Hanay, M. S.; Leblebici, Y.; Alaca, B. E. Piezoresistive silicon nanowire resonators as embedded building blocks in thick soi. *J. Micromech. Microeng.* **2018**, *28*, 045006.
(44) Wollschläger, N.; Tasdemir, Z.; Häusler, I.; Leblebici, Y.; Österle, W.; Alaca, B. E. Determination of the elastic behavior of silicon nanowires within a scanning electron microscope. *J. Nanomater.* **2016**, *2016*, 4905838.
(45) van Duin, A. C.; Strachan, A.; Stewman, S.; Zhang, Q.; Xu, X.; Goddard, W. A. ReaxFFSiO reactive force field for silicon and silicon oxide systems. *J. Phys. Chem. A* **2003**, *107*, 3803−3811.
(46) Khalilov, U.; Neyts, E.; Pourtois, G.; van Duin, A. C. Can we control the thickness of ultrathin silica layers by hyperthermal silicon oxidation at room temperature? *J. Phys. Chem. C* **2011**, *115*, 24839−24848.
(47) Neyts, E.; Khalilov, U.; Pourtois, G.; van Duin, A. Hyperthermal oxygen interacting with silicon surfaces: adsorption, implantation, and damage creation. *J. Phys. Chem. C* **2011**, *115*, 4818−4823.
(48) Khalilov, U.; Pourtois, G.; van Duin, A.; Neyts, E. Hyperthermal oxidation of Si (100) 2× 1 surfaces: effect of growth temperature. *J. Phys. Chem. C* **2012**, *116*, 8649−8656.
(49) Newsome, D. A.; Sengupta, D.; Foroutan, H.; Russo, M. F.; van Duin, A. C. Oxidation of silicon carbide by O2 and H2O: a ReaxFF reactive molecular dynamics study, Part I. *J. Phys. Chem. C* **2012**, *116*, 16111−16121.
(50) Khalilov, U.; Pourtois, G.; van Duin, A.; Neyts, E. On the c-Sil a-SiO2 interface in hyperthermal Si oxidation at room temperature. *J. Phys. Chem. C* **2012**, *116*, 21856−21863.
(51) Zimmerman, J. A.; WebbIII, E. B.; Hoyt, J.; Jones, R. E.; Klein, P.; Bammann, D. J. Calculation of stress in atomistic simulation. *Modell. Simul. Mater. Sci. Eng.* **2004**, *12*, S319.
(52) Piscanec, S.; Cantoro, M.; Ferrari, A.; Zapien, J.; Lifshitz, Y.; Lee, S.; Hofmann, S.; Robertson, J. Raman spectroscopy of silicon nanowires. *Phys. Rev. B: Condens. Matter Mater. Phys.* **2003**, *68*, 241312.
(53) Chen, J.; Conache, G.; Pistol, M.-E.; Gray, S. M.; Borgström, M. T.; Xu, H.; Xu, H.; Samuelson, L.; Håkanson, U. Probing strain in bent semiconductor nanowires with Raman spectroscopy. *Nano Lett.* **2010**, *10*, 1280−1286.
(54) Meier, R. J. On art and science in curve-fitting vibrational spectra. *Vib. Spectrosc.* **2005**, *39*, 266−269.
(55) Marola, S.; Bosia, S.; Veltro, A.; Fiore, G.; Manfredi, D.; Lombardi, M.; Amato, G.; Baricco, M.; Battezzati, L. Residual stresses in additively manufactured AlSi10Mg: Raman spectroscopy and X-ray diffraction analysis. *Mater. Des.* **2021**, *202*, 109550.
(56) Liou, H.-C.; Pretzer, J. Effect of curing temperature on the mechanical properties of hydrogen silsesquioxane thin films. *Thin Solid Films* **1998**, *335*, 186−191.
(57) Kakiuchi, H.; Ohmi, H.; Harada, M.; Watanabe, H.; Yasutake, K. Highly efficient oxidation of silicon at low temperatures using atmospheric pressure plasma. *Appl. Phys. Lett.* **2007**, *90*, 091909.
(58) Poborchii, V.; Tada, T.; Kanayama, T. Study of stress in a shallow-trench-isolated Si structure using polarized confocal near-UV Raman microscopy of its cross section. *Appl. Phys. Lett.* **2007**, *91*, 241902.
(59) Khalilov, U.; Pourtois, G.; Bogaerts, A.; van Duin, A. C.; Neyts, E. C. Reactive molecular dynamics simulations on SiO 2-coated ultrasmall Si-nanowires. *Nanoscale* **2013**, *5*, 719−725.
(60) Khalilov, U.; Pourtois, G.; Huygh, S.; van Duin, A.; Neyts, E.; Bogaerts, A. New mechanism for oxidation of native silicon oxide. *J. Phys. Chem. C* **2013**, *117*, 9819−9825.
(61) Khalilov, U.; Bogaerts, A.; Neyts, E. C. Toward the understanding of selective Si nano-oxidation by atomic scale simulations. *Acc. Chem. Res.* **2017**, *50*, 796−804.
(62) Ohta, H.; Watanabe, T.; Ohdomari, I. Strain distribution around SiO2/Si interface in Si nanowires: a molecular dynamics study. *Jpn. J. Appl. Phys.* **2007**, *46*, 3277.
(63) Uematsu, M.; Kageshima, H.; Shiraishi, K.; Nagase, M.; Horiguchi, S.; Takahashi, Y. Two-dimensional simulation of pattern-dependent oxidation of silicon nanostructures on silicon-on-insulator substrates. *Solid-State Electron.* **2004**, *48*, 1073−1078.
(64) Hung, P.; Hong, N. Simulation study of polymorphism and diffusion anomaly for SiO2 and GeO2 liquid. *Eur. Phys. J. B* **2009**, *71*, 105−110.
(65) Meade, C.; Hemley, R. J.; Mao, H. High-pressure X-ray diffraction of SiO 2 glass. *Phys. Rev. Lett.* **1992**, *69*, 1387.
(66) Maras, E.; Trushin, O.; Stukowski, A.; Ala-Nissila, T.; Jónsson, H. Global transition path search for dislocation formation in Ge on Si (001). *Comput. Phys. Commun.* **2016**, *205*, 13−21.
(67) Ma, D.; Lee, C.; Au, F.; Tong, S.; Lee, S. Small-diameter silicon nanowire surfaces. *Science* **2003**, *299*, 1874−1877.
(68) Matteini, F.; Dubrovskii, V. G.; Rüffer, D.; Tütüncüoğlu, G.; Fontana, Y.; Morral, A. F. I. Tailoring the diameter and density of self-catalyzed GaAs nanowires on silicon. *Nanotechnology* **2015**, *26*, 105603.
(69) Pakzad, S. Z.; Esfahani, M. N.; Alaca, B. E. Molecular Dynamics Study of Orientation-dependent Tensile Properties of Si Nanowires with Native Oxide: Surface Stress and Surface Energy Effects. *2021 IEEE 21st International Conference on Nanotechnology (NANO)*, 2021; pp 370−373.


https://doi.org/10.1021/acsanm.2c02983
*ACS Appl. Nano Mater.* 2022, 5, 13276−13285